Mechanical characterization of planar springs for compact radiation pressure power meters

Alexandra B. Artusio-Glimpse*, Ivan Ryger, Paul Williams, Kyle Rogers, Daniel Rahn, Andrew Walowitz, John Lehman
National Institute of Standards and Technology, 325 Broadway, Boulder, CO

ABSTRACT

Counter to conventional methods of measuring laser optical power, radiation pressure-based power meters operate by reflection rather than absorption. This provides an opportunity for in situ, non-destructive total beam power measurement. Compact radiation pressure power meters designed to operate between a few tens and a few thousands of watts consist of a planar millimeter-scale spring-electrode-mirror component that deflects under radiation pressure from an incident beam. Spring constant, resonant frequency, and quality factor of microfabricated springs as well as coating-induced straining of the spring are the focus of this manuscript. We compare finite element models of the mechanical component with various measurements to inform future designs.

Keywords: radiation pressure, spring constant, metrology, laser power meter, mechanical resonance, film stress, high reflectivity mirror, micromachined optomechanical system (MOEMS)

1. INTRODUCTION

High power CW lasers are controllable heat sources with many advantages for metal working applications. In welding, for example, lasers offer deep, narrow weld due to the high power density of the laser beam. These features are valuable in bonding processes[1], welding of thick metal sheets[2], welding of dissimilar metals[3], and other notable processes[4]. In addition, laser welding can operate at high feed rates and can be automated when systems are adequately instrumented. Weld quality is directly related to laser process parameters (power, raster speed, and wavelength), substrate temperature, and material, and much research is aimed at better understanding these relationships[5]. The most convenient free parameter for process control is laser power. Currently, there are two techniques for measuring laser power in weld systems; direct substitution and in situ sampling. Direct substitution is capable of high accuracy, but excludes the laser from other use. In situ sampling is less accurate, but provides real-time information. Quality monitoring within laser weld systems would be greatly improved if highly accurate power meters could also measure power in real time. For this reason, we are currently developing compact radiation pressure-based power meters that integrate with high power laser systems such as laser weld heads with the goal to achieve real time, absolute power measurements.

A multi-kilowatt Radiation Pressure Power Meter (RPPM) was recently developed that established a new methodology for primary standard laser power measurements[6,7]. The principle leverages the momentum transfer of photons to a highly reflective surface by measuring the force imparted to the mirror, expressed

$$F = (2Pr/c)\cos(\theta) \tag{1}$$

where P is the power of a beam incident on the mirror at an angle θ, c is the speed of light, and $r = R + \alpha(1-R)/2$ accounts for the fact that a reflected photon imparts two times its momentum whereas a photon absorbed imparts one time its momentum, where R is the reflectivity of the mirror and α is the fraction of non-reflected light that is absorbed.

The RPPM system is simple (composed of only a high reflectivity mirror, a precision force transducer, and a housing to limit air currents), it is non-destructive to the incident beam, and it returns a measure of optical power that is traceable to the kilogram (SI base unit). This system has even been used to demonstrate in situ measurements of power in a laser weld system[8]. Ideally suited for power levels above 10 kW, this meter is, however, limited by vibration noise at lower power levels[6,9]. In addition to that, the RPPM is large (30 cm on a side) relative to, say a laser weld head, making it inconvenient for seamless system integration.

*alexandra.artusio-glimpse@nist.gov; phone 1 303 497-5661; www.nist.gov/programs-projects/photoforce-project

By replacing the commercial force transducer at the heart of the RPPM with a more compact capacitive sensor, we are able to dramatically reduce the total size of this power meter (to approximately 5 cm on a side) while improving sensitivity, decreasing response time, and rejecting inertial noise sources (including vibration and gravity[10]). The capacitive pressure sensor is built from two identical planar spring electrodes with high reflectivity mirrors deposited on the outside surface of each spring (see Figure 1). The separation of the electrodes is determined from the capacitance between them. The momentum of the laser beam as it is incident on the mirror will push that electrode toward the other. The resulting change in separation of the electrodes is measured and related back to incident power by the spring constant of the spiral legs supporting the mirror and the geometry of the electrodes.

Inertial forces that are common to the two springs produce no signal, while asymmetric forces, such as that from a laser incident on the mirror of just one spring, change the inter-plate spacing and produce a signal. The magnitude of this signal depends on many factors like the electrical components of the capacitive bridge, mounting of the two planar springs, reflectivity of the mirrors, angle of incidence of the beam, and stiffness of the springs[11]. In this manuscript, we narrow our attention to just the mechanical planar springs. We present the architecture of two similar spring designs, report expected characteristics based on finite element models, and compare with measurements of spring stiffness, resonant frequency, quality factor, and residual strain post-release of fabricated components.

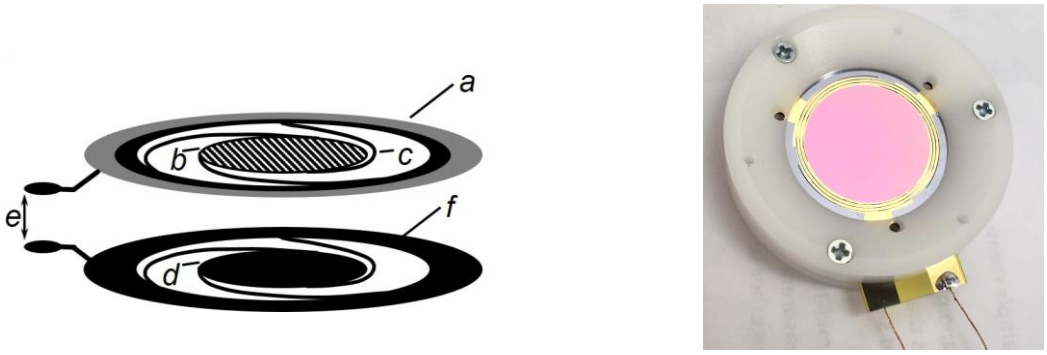

Figure 1. (left) Schematic of the dual spring radiation pressure sensor. Each spring, fabricated from a silicon wafer, consists of a supporting annulus *a* used to clamp the springs over a polyimide foil spacer, a high reflectivity mirror *b* connected to the annulus by three Archimedean spiral legs *c*, a disk electrode located on the back surface of the mirror *d* with electrical contacts *f* such that capacitance measurements are made between electrodes *e*. (right) Photograph of a mounted pair of springs with high reflectivity mirror designed for 1070 nm laser incident at 45°.

2. METHODS AND RESULTS

2.1 Spring fabrication

The planar springs in this study are made from crystalline silicon wafers. General fabrication steps are outlined in Figure 2 beginning with a 380 µm thick double side polished silicon wafer. We first deposit a high reflectivity mirror that is optimized for peak reflectivity at our operating wavelength of 1070 nm with an angle of incidence of 45° and random polarization (optimized for the average of transverse electric and transverse magnetic polarization states). Two mirror types are studied in this manuscript and each are paired with a spring of different stiffness. We will henceforth refer to each spring design and mirror combination as Spring 1 and Spring 2, as detailed in Table 1. The mirror of Spring 1 is a commercially deposited distributed Bragg reflector using ion beam sputtering (IBS) of approximately 16 alternating pairs of tantalum pentoxide (Ta_2O_5) and silicon dioxide (SiO_2) with a total thickness of approximately 6.5 µm and peak reflectivity of 0.99997. The mirror of Spring 2 is our in-house deposited Bragg reflector on top of 200 nm of e-beam deposited gold. In-house, we use plasma-enhanced chemical vapor deposition (PECVD) to put down 4 alternating pairs of amorphous silicon (a-Si) and silicon dioxide (SiO_2) layers with a total thickness of 1.1 µm and peak reflectivity of 0.9992. Following deposition, the mirror is plasma etched to leave only a 20 mm diameter island at the center of each spring.

Table 1. Design summary of two planar silicon springs studied in this manuscript. (*exact thickness of IBS mirror is not known.)

	Mirror	**Leg Width**
Spring 1	IBS, Ta_2O_5/SiO_2, 6.5 µm thick*	265 µm
Spring 2	PECVD, a-Si/SiO_2, 1.1 µm thick	425 µm

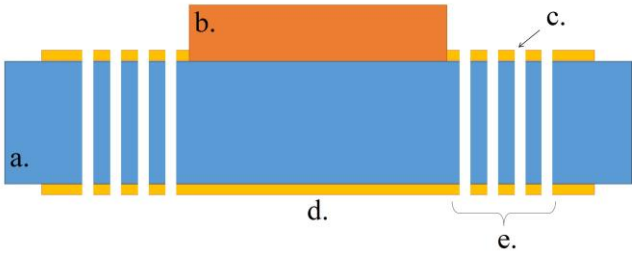

Figure 2. Cross-section of the planar silicon spring with fabrication steps beginning with a double side polished silicon wafer (a.). On to one side, a high reflectivity distributed Bragg reflector is deposited (b.), then thermal strain balancing gold (c.) is evaporated over the front side of the wafer while a gold electrode is deposited on the back side of the wafer (d.). Lastly, spiral legs are etched through the wafer by deep reactive ion etching to form the planar spring (e.).

Following mirror deposition and etching, 200 nm thick gold electrodes are deposited and patterned on the back side of the wafer. Due to the difference in thermal expansion coefficient of gold and silicon, the mirror is masked and a matching layer of gold is deposited on the top side of the wafer's spring legs to suppress their bending when heated by optical absorption of the incident laser light. The last step in the fabrication process is deep reactive ion etching (DRIE) of the silicon wafer through its thickness. This creates three spring legs in the form of an Archimedean spiral that surround the mirror and terminate at an arc length of $4\pi/3$, totaling 45 mm long. Spring 1 is a softer spring design with 265 µm wide legs. Spring 2 is a stiffer spring design with 425 µm wide legs. This deep etch step also cuts the circular chips out of the whole wafer with 32 mm diameter (3 chips per wafer).

2.2 Resonant frequency and quality factor

In this section, we look at the primary resonance of each spring-mass design. To do this, we mounted a pair of Spring 1 chips and a pair of Spring 2 chips (like the photograph in Figure 1), where the chips are spaced by a 42 µm polyimide foil. A fast (1 kHz) dual arm interferometer with 1.24 nm resolution recorded a time series of the position of each spring simultaneously. By calculating the discrete Fourier transform of each time series and locating the first major resonant peak, we generated the plots in Figure 3. We use Lorentzian fits to determine the resonant frequency and quality factor of each spring design. Spring 1 fit to a resonant frequency of 75.4403 ± 0.0002 Hz and quality factor of 680 ± 2. Spring 2 fit to the resonant frequency 111.6918 ± 0.0004 and quality factor 242.1 ± 0.6. Throughout this paper, we will consistently express uncertainty bounds with "±" as given by the standard error of a fit parameter or standard deviation of a sequence of measurements with a coverage factor of 2. Clearly visible in the plots of Figure 3, two springs of the same design that are clamped together are identical oscillators, as shown by the overlapping measured resonance curves for the left and right springs.

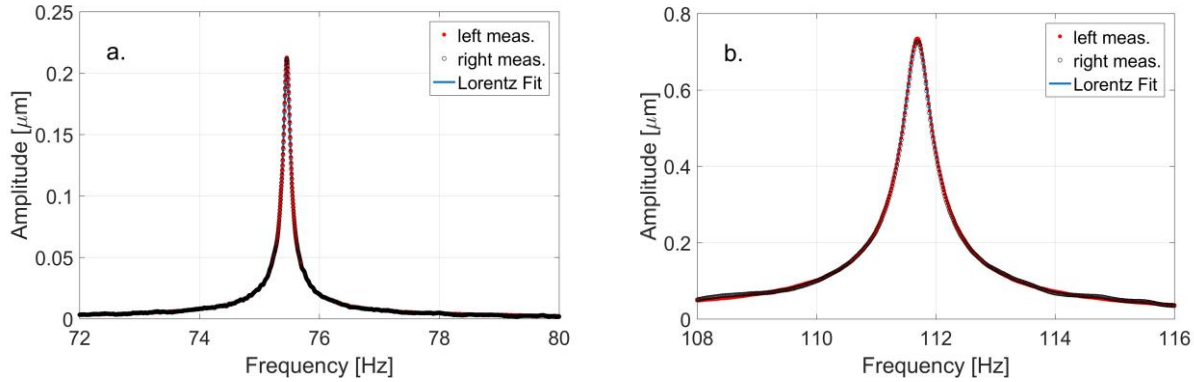

Figure 3. Measured resonance of (a.) Spring 1 and (b.) Spring 2 with Lorentz fit determining a resonant frequency of (a.) 75.4403 ± 0.0002 Hz and (b.) 111.6918 ± 0.0004 Hz and quality factor (a.) 680 ± 2 and (b.) 242.1 ± 0.6.

2.3 Spring stiffness

We measure the spring stiffness of each planar spring by deflecting the spring with calibrated masses and measuring this deflection with an interferometer (100 nm resolution). In Figure 4, we plot the measured deflection of each spring against the gravitational force of each mass, where each data point is the mean of 20 mass measurements and 10 deflection measurements and error bars are two times the standard deviation of those. The model we want to solve is $F = kx$ to determine the spring constant k, yet we know the uncertainty in x, the measured deflection, is larger than the uncertainty in F, the measured weight of each mass. Therefore, we solve the linear model $x = bF$, where $b = 1/k$, and propagate uncertainty according to the GUM procedure. Notably, fit residuals are randomly distributed about zero, indicating the springs are indeed linear in this deflection range.

A finite element model of each spring geometry with built-in crystalline silicon material parameters substrate (Young's modulus = 179 GPa, Poisson's ratio = 0.27, density = 2329 kg/m^3), excluding the influence of gravity, predicts the spring stiffness to be 76.6 N/m and 171 N/m for Spring 1 and Spring 2. Both model geometries over predict the spring stiffness by 8% relative to measured stiffness values of 71 ± 1 N/m and 158.2 ± 0.4 N/m for each spring. Importantly, the discrepancy between measured and modeled spring stiffness is the same for each spring geometry meaning we can refine the model with improved material parameters.

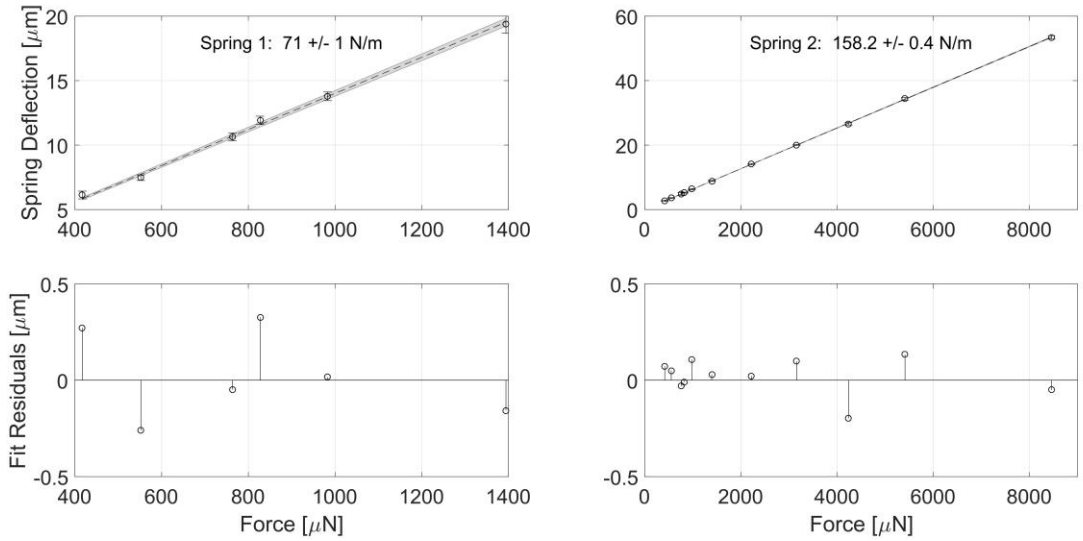

Figure 4. (top) Measured spring deflection versus weight of measured masses with linear fit. (bottom) Random distribution of fit residuals show no need for higher order stiffness terms.

2.4 Strain from mirror coating – model

We find that the high compressive stress of the thick IBS mirror on Spring 1 deforms the silicon legs of that spring design to such a degree that capacitance calibration of the chips is unsuccessful due to high rates of pull-in[12] as the plates are too closely positioned when clamped. We hypothesize that the compressively stressed film imparts permanent strain on the spring legs resulting in an effective sagging of the electrode (the electrode moves out of the plane of the spring). We also expect the mirror stress leads to bowing of the central disk of silicon that supports both the mirror and the central electrode. This bowing will lead to divergence from the parallel plate capacitor approximation.

We are limited in mechanical measurement capability to fully study this stress effect; therefore, multiphysics models were employed to add insight to the supposed impact of the mirror stress on the spring mechanics. In the following, the solid mechanics model given an initial thin film stress is investigated to argue for or against the hypothesis that the compressively stress mirror will result in sagging of the chip electrodes and may lead to deformations of the electrodes.

Firstly, the mirror stress is not precisely known. Fortunately, we have thick witness fused silica wafers with the same IBS mirror coating. With a laser-based wafer curvature measurement system, we measure the curvature of the witness mirrors and, using Stoney's film stress equation (2), are able to extract a prediction of film stress. We know the wafer thickness, we can estimate the film thickness, we know Young's modulus, and Poisson's ratio of the fused silica wafers and are able to use Stoney's equation to estimate the stress of the IBS mirror from measurements of the post-coated wafer curvature with the caveat that we must assume the wafers were perfectly flat prior to coating.

$$\sigma_f = \frac{E_s h_s^2 \kappa}{6 h_f (1-\nu_s)} \tag{2}$$

Stoney's film stress equation gives stress of a thin film of height h_f = 6.5 µm on a thick substrate of height h_s = 1 mm with Young's modulus E_s = 73 GPa and Poisson ratio ν_s = 0.17 giving rise to a measureable surface curvature (change before and after film deposition) κ = -0.083 1/m. From this, we approximate the stress of the mirror coating is σ_f = -188 MPa.

A finite element model of Spring 1 (with 265 µm wide legs) was built with the mirror film (modeled with material parameters of silicon dioxide) on the top side of the central disk of the spring (gravity excluded). Figure 5 shows the vertical displacement field of the strained silicon spring due to the compressively stressed mirror coating. The maximum displacement of the electrode is -27 µm at the edges of the central disk. The center of the disk is 10 µm higher than its edges leading to a curvature of 0.2 1/m.

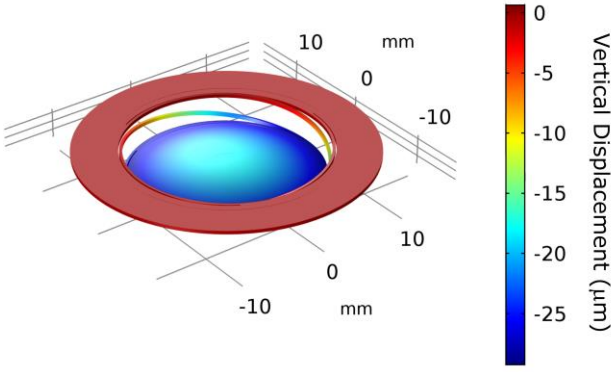

Figure 5. Spring 1 deformation due to 6.5 µm thick, -188 MPa compressively stressed silicon dioxide on the top surface of the central disk of the silicon spring. In the image, deformation in the vertical direction is exaggerated 100X for visibility, while the color map gives the modeled sag in units of microns. This finite element model predicts a maximum vertical displacement of -27 µm at the edges of the central disk and a bow height of 10 µm above that at the center of the disk, corresponding to a curvature of -0.2 1/m (optically equal to a focal length of -2.5 m).

For comparison, we repeated the model for Spring 2, which has wider legs (425 µm), while keeping the same IBS mirror parameters in the model. In this case, maximum vertical displacement in the model is -17 µm and the disk curvature is 0.13 1/m. Wider spring legs are less deformed by the same mirror and the deformation is not linear with spring stiffness. We also compare the relatively thick IBS mirror to our in-house PECVD mirror that is one quarter the thickness of the former, though, is deposited with higher stress at roughly -234 MPa (measured by pre- and post-coated wafer bow and solving of Stoney's equation). At just 1.1 µm thick, this mirror produces less strain so that the central disk maximum displacement is predicted to only be -8 µm with a curvature of 0.045 1/m. In theory and in the model, deformation from the compressive mirror coating is perfectly eliminated with the addition of a stress matching film on the opposite side of the central disk to balance the stress of the mirror; though, in practice perfect stress balancing can only be approached.

2.5 Strain from mirror coating – measurement

The above models loosely agree with observations of the fabricated springs. Three spring chips are measured with an optical profilometer as the spring rests on an annulus mount such that the central disk of the spring may sag under gravity. These three chips are selected for their different designs: 1. Spring 1 without the mirror film. 2. Spring 1 with thick IBS mirror film. 3. Spring 2 with PECVD mirror. Analysis of these measurements follow.

Measured line profiles through the center of each chip from edge to edge of the annulus are plotted in Figure 6. The weight of the silicon disk under gravity pulls the soft spring (71 N/m) down by about 66 µm (mean of two minimums in smoothing spline fit to data – orange solid line in Figure 6). Adding a thick mirror worsens this sag by an additional 42 µm. For comparison, the stiffer spring (158 N/m) having a mirror one quarter the thickness of the thick IBS mirror, sags by roughly 25 µm. Theoretically, we expect the gravity sag of a 2X stiffer spring to be one half that of the soft spring (i.e. 30 µm) and the thinner mirror should add to that deflection at edges of the central disk (an additional 8 µm if we believe the model above). Due to the noise in the measured profile of each spring (primarily due to stitching errors), it is difficult to get a good estimate of the true sag of each spring. Nevertheless, these estimates are helpful for supporting the results from modeling. Note, we can safely ignore the weight of the mirror and its contribution to sag under gravity because the mass of the thick IBS mirror is approximately 2% the mass of the silicon disk and is well within the uncertainty of this measurement.

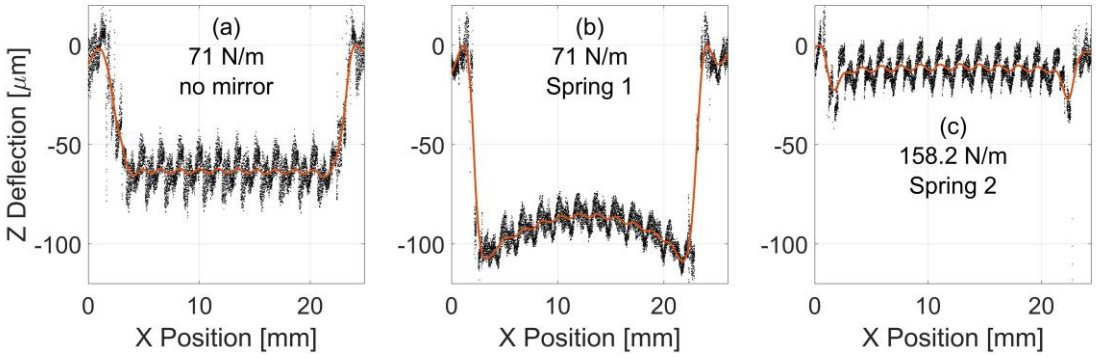

Figure 6. Optical profiles of three springs (with spring constant denoted): (a) Spring 1 with no mirror sags by 66 µm under gravity, (b) Spring 1 with the compressively stressed thick IBS mirror sags by 108 µm from gravity and the additional pull from the mirror, and (c) Spring 2 (2X stiffer with a mirror 1/4th as thick) sags by an approximate 25 µm. (dots) raw data, (orange line) cubic spline smoothing line fit.

Looking closely at the central disk of each chip where the mirror is located, we determine the disk curvature and peak bow height and predict the stress of each mirror. As expected the chip with no mirror on the central disk is measured to be perfectly flat across this area. On the other hand, the two chips with mirrors do show bowing upward, suggestive of compressive stress in a film placed on the top surface of the silicon substrate.

As seen in Figure 7, the thick IBS mirror results in significant bowing of the central disk. By fitting all the data from three line scans across the chip center to a circle, we find the radius of curvature is -0.463 ± 0.005 1/m with a peak bow height at the center of 23.1 ± 0.2 µm. This is twice as large as predicted in the above model. If we apply Stoney's equation (2) with the new measurement of curvature and use coefficients of a silicon substrate (E_s = 179 GPa, ν_s = 0.27, h_s = 380 µm), we predict that the mirror film has a stress of -420 ± 4 MPa.

An additional factor to consider is the tension of the spring legs on the central disk. From the fit of a circle to the data, we know the radius of curvature (2.16 ± 0.02 m) is much larger than the peak bow height, which means the arc length of the circular segment defined by the disk diameter is nearly equal to the chord length of this segment. Thus, the lateral displacement of the disk edges inwards is exceptionally small, approximately 5 µm at each edge. The effective spring constant for displacement of the spring legs in the plane of the chip is roughly two times stiffer than for the normal out-of-plane movements (based on finite element models). From this, we can estimate the tension of the spring legs on the bowed central disk as (-158 N/m)(-5 µm) = 0.8 mN, and by accounting for the contact area of the three legs on the disk the pressure is 3 kPa, or reasonably small to ignore when compared to the predicted mirror stress.

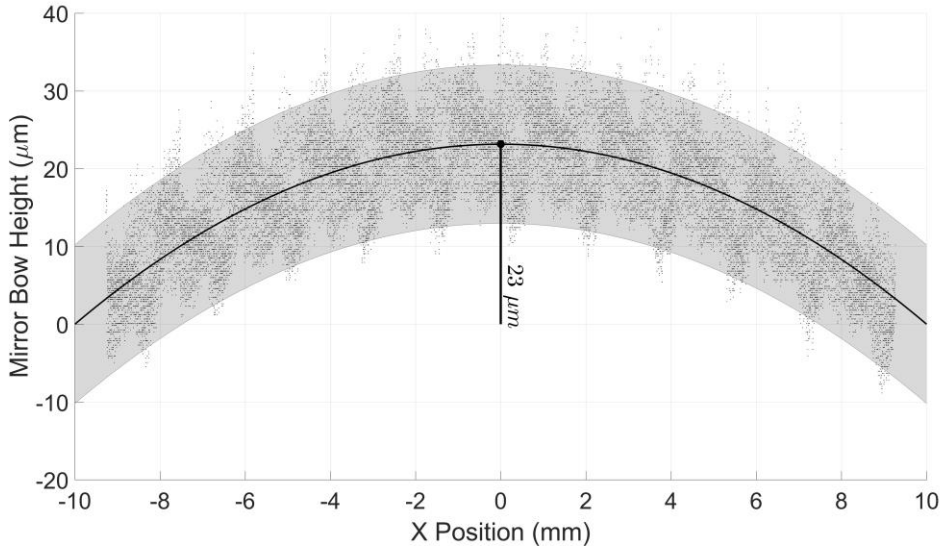

Figure 7. IBS mirror bow on Spring 1 measured at three locations near the center of the chip with circle fit (black line) and 2 times the standard deviation of the fit residuals (gray shaded region). Expected bow height value is 23.1 ± 0.2 µm and the expected curvature is -0.463 ± 0.005 1/m.

Similar calculations are carried out for the stiffer sample with PECVD mirror (see Figure 8). The measured peak bow height of this central disk is 1.8 ± 0.5 µm and measured curvature is -0.0354 ± 0.009 1/m. This leads to a predicted mirror stress of -190 ± 50 MPa. Using the curvature measurement system with a ø75 mm wafer fully coated with the PECVD mirror, the mirror stress is measured to be -234 ± 3 MPa, given by the mean and standard deviation of 100 measurements taken across the diameter of the wafer. These measurements indicate that the PECVD mirror process results in films that have intrinsically slightly higher stress than the IBS processed films, but that the difference in thickness has a larger impact on strain of the underlying silicon disk. The large discrepancy between predicted stresses from the two measurement methods, though, indicates these techniques are highly inaccurate and may only be considered as representative of the truth.

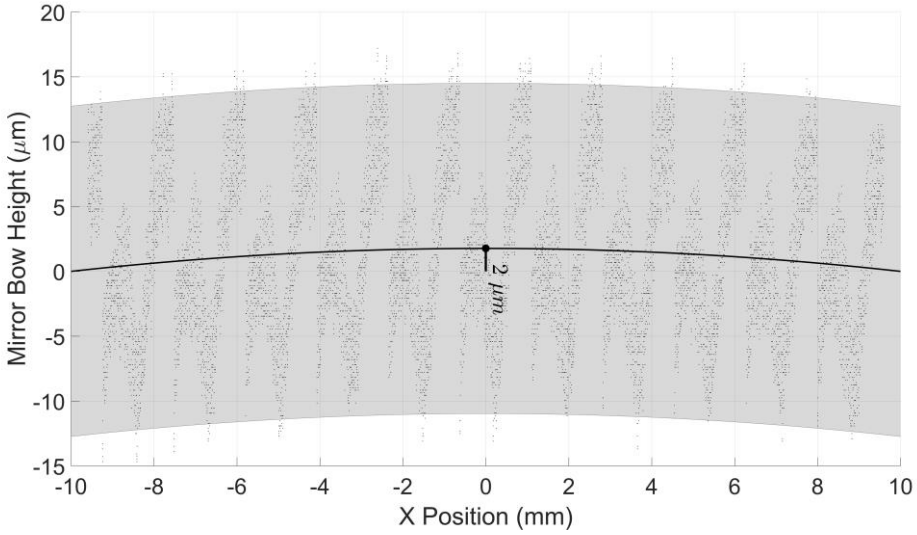

Figure 8. Bow height of PECVD mirror on Spring 2 measured at one location near the center of the chip. The estimated peak bow height at the center of the mirror is 1.8 ± 0.5 μm and the curvature is -0.0354 ± 0.009 1/m based on a fit of the data to a circle.

3. CONCLUSION

Planar spiral springs made from silicon with gold electrodes and high reflectivity mirrors have been fabricated. We study various mechanical features of two spring designs (one soft with a thick, high stress mirror and one stiff with a thin, high stress mirror) and find that two springs of the same design when clamped together with a thin polyimide foil defining their separation are identical resonators with a resonant frequency of 75 Hz or 112 Hz, respectively. We find the quality factor of each spring design is different, even though the silicon substrate of each spring is the same: 680 for Spring 1 and 242 for Spring 2. This difference in quality factor may be related to the strain of each spring imposed by the compressive stress in the dielectric stack that makes up the high reflectivity mirror centrally positioned on the spring. A finite element study of this straining indicates a compressively stressed film on one side of the central disk of one spring will lead to stretching of the spring downwards as well as bowing of the central disk upwards. The degree of bending and bowing depends on the spring stiffness and thickness of the compressive mirror. Optical profile measurements (with high noise and stitching errors) indicate that the mirror stretches the spring downwards (toward the electrode side of the chip) beyond sagging from gravity, while measurements of curvature of the central disk indicate that the stress of the mirror coating is in the range of -190 MPa and -420 MPa. We additionally calibrate the stiffness of each spring and test its linearity by placing known masses on the spring and measuring deflection with an interferometer. Over a deflection range of 20 μm or 60 μm, we find no sign of nonlinearity in the spring constant. We also compare the measured spring constants (71 N/m and 158 N/m) to finite element models and find that the model consistently over predicts the spring constant by 8% due to slight differences in material parameters. As we continue to develop compact radiation pressure sensors for laser power measurement, we will apply the measurements reported in this manuscript to inform our models and future designs. Due to the large difference in refractive index between the materials (a-Si and SiO2) used in the PECVD mirror, we are able to coat a thinner mirror with just a small reduction in reflectivity. This minimizes the strain on our springs. Until a solution is formulated to relax the stress in the mirror coating or balance its impact on straining of the spring, the PECVD mirror is preferred over the IBS mirror because spring strain by the latter causes high rates of pull-in of the capacitor plates in our devices. In addition, this work establishes a robust technique for measuring spring stiffness – an important parameter for validations of our compact radiation pressure power meter devices.

identification does not imply recommendation or endorsement by the National Institute of Standards and Technology, nor does it imply that the materials or equipment identified are necessarily the best available for the purpose.

REFERENCES

[1] Benyounis, K. Y., Olabi, A. G., and Hashmi, M. S. J., "Effect of laser-welding parameters on the heat input and weld-bead profile," Journal of Materials Processing Technology 164-165, 978-985 (2005).

[2] Zhang, M., Chen, G., Zhou, Y., and Liao, S., "Optimization of deep penetration laser welding of thick stainless steel with a 10 kW fiber laser," Materials and Design 53, 568-576 (2014).

[3] Mai, T. A. and Spowage, A. C., "Characterisation of dissimilar joints in laser welding of steel-kovar, copper-steel and copper-aluminium," Materials Science and Engineering A 347, 224-233 (2004).

[4] Cary, H. B. and Helzer, S., [Modern Welding Technology], Prentice Hall, Upper Saddle River, NJ (2004).

[5] Fotovvati, B., Wayne, S. F., Lewis, G., and Asadi, E., "A Review on Melt-Pool Characteristics in Laser Welding of Metals," Advances in Materials Science and Engineering 4920718, (2018).

[6] Williams, P., Hadler, J., Maring, F., Lee, R., Rogers, K., Simonds, B., Spidell, M., Stephens, M., Feldman, A., and Lehman, J., "Portable, high-accuracy, non-absorbing laser power measurement at kilowatt levels by means of radiation pressure," Optics Express 25(4), 4382 (2017).

[7] Williams, P., Hadler, J., Simonds, B., and Lehman, J., "Onsite multikilowatt laser power meter calibration using radiation pressure," Applied Optics 56(34), 9596 (2017).

[8] Williams, P., Sowards, J., and Simonds, B., "A novel optical laser-power measurement technique offers high accuracy in real time," Welding Journal, 30-34, (March 2016).

[9] Williams, P., Hadler, J., Ryger, I., Artusio-Glimpse, A., King, D., Vo, T., and Lehman, J., "Radiation-Pressure Enabled Traceable Laser Sources at High CW Powers," submitted IEEE Transactions on Instrumentation & Measurement.

[10] Artusio-Glimpse, A. B., Ryger, I., Williams, P., and Lehman, L., "Non-Absorbing, Point-of-Use, High-Power Laser Power Meter," Applied Industrial Optics: Spectroscopy, Imaging and Metrology, Paper# ATh2A.2 (2018).

[11] Ryger, I., Artusio-Glimpse, A. B., Williams, P., Tomlin, N., Stephens, M., Rogers, K., Spidell, M., and Lehman, J., "Micromachined force scale for optical power measurement by radiation pressure sensing," accepted to IEEE Sensors.

[12] Bao, M., [Analysis and Design Principles of MEMS Devices], Elsevier B. V., Amsterdam, Boston, Heidelberg, London, New York, Oxford, Paris, San Diego, San Francisco, Singapore, Sydney, & Tokyo, 181-184 (2005).